

# EPR Oxygen Mapping (EPROM) of Engineered Cartilage Grown in a Hollow-Fiber Bioreactor

Scott J. Ellis,<sup>1,2</sup> M. Velayutham,<sup>3</sup> S. Sendhil Velan,<sup>1</sup> Erik F. Petersen,<sup>1</sup> Jay L. Zweier,<sup>3</sup> Periannan Kuppasamy,<sup>3</sup> and Richard G.S. Spencer<sup>1\*</sup>

**A novel electron paramagnetic resonance (EPR)-based oxygen mapping procedure (EPROM) is applied to cartilage grown in a single-, hollow-fiber bioreactor (HFBR) system. Chondrocytes harvested from the sterna of 17-day-old chick embryos were inoculated into an HFBR and produced hyaline cartilage over a period of 4 weeks. Tissue oxygen maps were generated according to the EPROM technique (Velan et al., Magn Reson Med 2000;43:804–809) by making use of the line-broadening effects of oxygen on the signal generated from nitroxide spin probes. In addition, the effect on oxygen consumption of the addition of cyanide to the tissue was investigated. Cyanide is a potent inhibitor of oxidative phosphorylation, and accordingly, given the constant provision of oxygen to the tissue, it would be expected to increase oxygen levels within the HFBR. The EPROM measurements showed a significant increase in oxygen concentration in the cartilage after the addition of cyanide. In contrast to other methods for studying oxygen in cartilage, EPROM can provide direct, noninvasive visualization of local concentrations in three dimensions. Magn Reson Med 46: 819–826, 2001. © 2001 Wiley-Liss, Inc.**

**Key words:** EPR; cartilage; chondrocytes; oximetry; oxygen mapping

Although cartilage relies mainly upon anaerobic glycolysis for energy production (1), aerobic cellular respiration is also used to a considerable extent and is vital to optimal function. For example, chondrocytes in culture need approximately 20% oxygen in the gas phase to produce ideal growth (2) and DNA synthesis is depressed at low oxygen levels (3). The degree of aerobic metabolism may also be strongly coupled to the quantity and quality of glycosaminoglycan and collagen production (4).

Indeed, there exists a complex interplay between glycolysis and aerobic respiration in cartilage. The availability of low concentrations of oxygen to chondrocytes has been shown to reduce glycolysis, in accordance with a negative Pasteur effect (5). Other studies have provided evidence that glucose utilization increases under hypoxic conditions in monolayer (2,6) and 3D (4) cultures and explant tissue (7), consistent with a positive Pasteur effect. It has also been found that articular cartilage exposed to low concentrations of glucose increases its oxygen utilization considerably (4,8).

Chondrocytes in articular cartilage and in the intervertebral disc (two largely avascular tissues) face steep gradients of oxygen and other nutrients (7). Eliciting patterns of oxygen consumption in these tissues may be an important component of understanding the metabolism of cartilage at various tissue depths (3,4,6,7,9–11).

In vitro cartilage constructs provide an ideal setting for studying cartilage, allowing for the analysis of metabolic parameters under carefully controlled conditions. Most such studies utilize 2D cell culture systems. However, such systems do not reflect the structure of solid cartilage, in which chondrocytes are embedded in a dense matrix comprised primarily of proteoglycan and collagen (12). In contrast, 3D culture systems (13), including the hollow-fiber bioreactor (HFBR) we used previously (14–18), provide a more realistic diffusion barrier between cells and their nutrient supply and permit interaction between chondrocytes and extracellular matrix (ECM). 3D culture systems also support the chondrocyte phenotype, rather than potentiating the dedifferentiation of chondrocytes into fibroblasts (19–21). Thus, our previous work on engineered cartilage tissue centered on an HBFR system that produced macroscopic amounts of matrix, and in which the chondrocytes maintained their phenotype (14–18). Various invasive methods have been employed to study oxygen metabolism in cartilage. These include the introduction of microelectrodes into chondrocytes in cell culture (22), cartilage explants (23), and in vivo cartilage tissue (24). Other studies attempted to indirectly estimate articular cartilage oxygen by measuring the oxygen tension of synovial fluid (25). Quantitative values of oxygen uptake by growth plate chondrocytes have been obtained using the Pd-coproporphyrin phosphorescence quenching technique (11,26). The Warburg technique (27–29), which calculates oxygen consumption based on measurements of pressure and volume changes in a closed system, has also been applied to articular cartilage (8).

Electron paramagnetic resonance (EPR) spectroscopy and imaging are powerful techniques for monitoring metabolic activity, redox state, and oxygen concentration in tissues (30–32). EPR oximetry, which employs a variety of soluble and particulate probes, has been used to measure the oxygen concentrations in living tissues, including brain, liver (33), and muscle (34). Particulate probes provide information about oxygen partial pressure (35,36), whereas soluble probes report dissolved oxygen concentration (36–38). EPROM (39) is a noninvasive technique for measuring and mapping local oxygen concentration. It also permits the quantitation of changes in oxygen concentration over time. It involves the creation of a 2- or 3D line-width map calculated directly from maps of spectral line amplitude and intensity. A calibration curve relating

<sup>1</sup>Nuclear Magnetic Resonance Unit, National Institute on Aging, National Institutes of Health, Baltimore, Maryland.

<sup>2</sup>School of Medicine, Johns Hopkins University, Baltimore, Maryland.

<sup>3</sup>EPR Center, Division of Cardiology, Department of Medicine, School of Medicine, Johns Hopkins University, Baltimore, Maryland.

\*Correspondence to: Richard G.S. Spencer, M.D., Ph.D., Chief, Nuclear Magnetic Resonance Unit, National Institutes of Health, NIA, Gerontology Research Center, 4D-06, 5600 Nathan Shock Drive, Baltimore, MD 21224. E-mail: spencer@helix.nih.gov

Received 3 January 2001; revised 6 April 2001; accepted 30 April 2001.

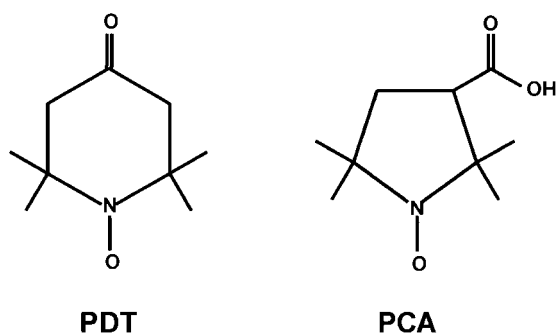


FIG. 1. Chemical structure of the oximetry and imaging nitroxide labels used in the cartilage bioreactor experiments. 4-oxo-2,2,6,6-tetramethylpiperidine- $d_{16}$ -N-oxyl: PDT; 3-carboxyl-2,2,5,5-tetramethylpyrrolidine-N-oxyl: PCA.

line-width to oxygen concentration then permits the line-width at a given voxel in an image to be converted to the local oxygen concentration.

Due to its noninvasive nature and its ability to monitor oxygen before and after intervention and to give spatially localized data, EPROM is an excellent technique for measuring oxygen in solid engineered cartilage tissue. Accordingly, phantom studies were carried out to define the capability of EPROM for oxygen mapping under conditions and geometry similar to those in the HFBR system. Then, EPROM was applied to cartilage tissue under control conditions and in response to an intervention which has a strong effect on oxygen utilization: the provision of cyanide. To our knowledge, this is the first report of oxygen mapping in a 3D cartilage system.

## MATERIALS AND METHODS

### Three-Concentric-Tube Phantom Construction

To assess the capabilities of EPROM in detecting oxygen concentration in a cylindrical geometry approximating that of a bioreactor, a phantom was constructed using three concentric tubes of varying diameters (innermost = 3 mm, middle = 11 mm, and outermost = 16 mm). All tubes were filled to a vertical height of 4 cm with 0.5 mM 4-oxo-2,2,6,6-tetramethylpiperidine- $d_{16}$ - $^{15}$ N-oxyl (perdeuterated tempone (PDT); CDN Isotopes, Quebec, Canada) (Fig. 1) dissolved in Dulbecco's phosphate-buffered saline. The inner- and outermost tubes were exposed to room air (21%, 224  $\mu$ M, oxygen). The middle tube was bubbled with 36% (385  $\mu$ M) oxygen, and sealed. The entire phantom was then placed vertically in the resonator for 3D spectral-spatial imaging.

### Bioreactor Construction and Inoculation

HFBRs were constructed as described previously (14–18) (Fig. 2) from high-purity glass tubing, with an inner diameter of 4 mm. Each reactor was fitted with a side port positioned at one end to allow for the injection of chondrocytes. A single porous polypropylene hollow fiber (inner diameter 330  $\mu$ m, 0.2  $\mu$ m pores; Microgen, Laguna Hills, CA) was positioned centrally along the length of the HFBR. The fiber was held in place on both ends of the glass

tube with biomedical-grade silicon rubber (MED-1137; NuSill Silicone Technology, Carpinteria, CA). Tubing (96400-14; Masterflex, Vernon Hills, IL) for tissue culture medium (TCM) influx and efflux was fitted on both sides of the bioreactor and connected to a reservoir.

Chondrocyte cultures were grown as previously described (14–18). Briefly, chondrocytes were isolated from the distal sterna of 17-day-old chick embryos using 4.5 mg/ml of a collagenase digest (Worthington, Freehold, NJ) for 3 h at 37°C with continual stirring. The chondrocytes were separated by centrifugation and then resuspended in TCM. The composition of the TCM has been detailed elsewhere (17). Each reactor was then inoculated with 30 million cells.

Immediately after inoculation, the bioreactors were placed in a 5%  $\text{CO}_2$ /95% air incubator maintained at 37°C. A pump interface (6484-10; Masterflex) incorporated into the perfusion loop was attached to a pin compression pump (Cellco, Germantown, MD) which constantly perfused the system with TCM.

The chondrocyte cultures within the HFBR were allowed to grow for 4 weeks, at which time the cells and matrix uniformly filled the inside of the HFBR.

### EPR Equipment and Methodology

All EPR experiments were performed with the previously described (40) L-band EPR imaging system. A ceramic three-loop, two-gap resonator with a central bore of 20 mm diameter was used for all experiments (39). The resonant frequency was 1.2 GHz.

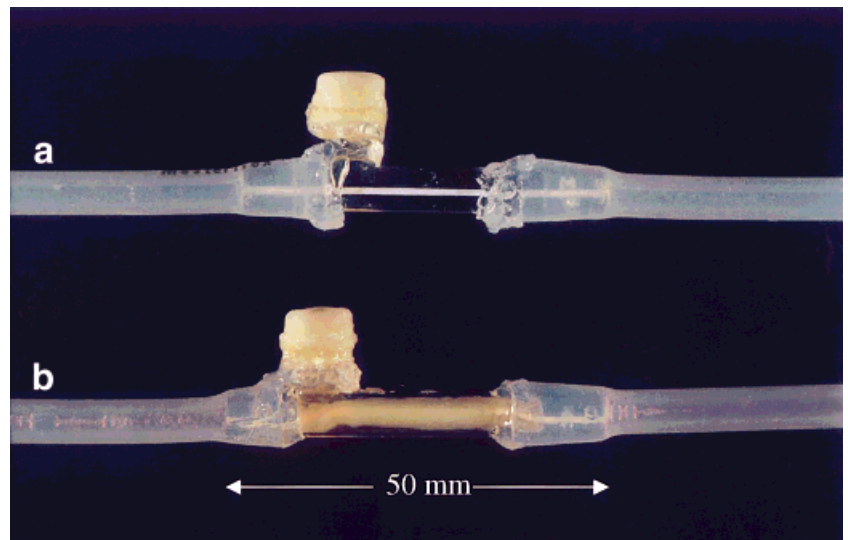
3D spectral-spatial data sets consisted of two spatial dimensions in the plane normal to the longitudinal axis of the bioreactor along with a spectrum corresponding to each resulting voxel. The maximum gradient strength,  $G_{\text{max}}$ , was 21.7 G/cm, and the modulation amplitude and frequency were 0.1 G and 100 kHz, respectively. Similar parameters were used for the phantom, calibration, and inhibition of cellular respiration (cyanide) components of the study. Data acquisition and processing were performed using a personal computer with custom software (39).

The spatial imaging experiments were performed either in two spatial dimensions (projected across the longitudinal axis of the reactor or phantom) or in three spatial dimensions. For these, as well as for the spectral-spatial images, rapid 2D spatial images were used to center the object in the resonator and to select optimal data acquisition parameters.

For all of the cartilage experiments, a total of  $24 \times 24 = 576$  projections defined by angularly-sampled gradient fields were acquired, with a total imaging duration of 1 h and 17 min. A field of view (FOV) of 4.0 G in the spectral dimension and 20 mm  $\times$  20 mm in the cross-sectional spatial dimension was employed. The cartilage construct was symmetric and measured 2.9 mm in diameter. The images were corrected for hyperfine artifacts (41) and reconstructed using filtered back-projection methods (42).

Spatial maps of spectral amplitude and intensity were then created. The amplitude map was obtained from the height of the absorption line at approximately the resonance field,  $B_0$ , for each voxel. The intensity map was obtained by computing the area of the absorption line

FIG. 2. Single-fiber bioreactor used to grow cartilage. Chondrocytes are injected via a syringe through the rubber membrane covering the injection port on the left side of the bioreactor. **a:** Empty bioreactor (before inoculation with cells). **b:** Bioreactor 17 days after inoculation. Cartilage has formed a cylindrically symmetrical sleeve around the single fiber.



corresponding to each voxel. An oxygen map was derived from the line-width of the signal at each voxel, in accordance with the EPROM procedure. Our display algorithm for depicting line-width gives increased brightness to broader lines.

Calibration

Calibration of oxygen-induced line-broadening as a function of oxygen concentration was performed separately to accurately relate line-widths to oxygen concentrations. A saline solution of 0.25 mM PDT was equilibrated with 11 different oxygen concentrations in the physiologic range. 3D spectral-spatial images were then obtained. The line-widths from the images were then used to construct the calibration curve.

Influx/Efflux Experiment in a Bioreactor Without Tissue

A series of 2D spatial images were acquired to determine the approximate time required for PDT to completely dis-

tribute into the HBFR. A bioreactor circuit without tissue but connected by tubing to a reservoir bottle was centered within the resonator. A peristaltic pump was used to perfuse the reactor with TCM containing 1.0 mM of PDT. Continuous acquisition of 2D spatial images began immediately after the initiation of perfusion; each image was acquired over 3 min and acquisition was terminated after the spin probe had diffused completely into the HFBR. To study the clearance of the label, the bioreactor circuit was then perfused with TCM without PDT. Images were again acquired every 3 min until no signal could be obtained.

Cartilage Experiments

3D Cartilage Experiments

An HFBR containing engineered cartilage was centered in the resonator and perfused with TCM containing 1.0 mM 3-carboxyl-2,2,5,5-tetramethylpyrrolidine-N-oxyl (PCA) (Fig. 1). Images of the cartilage were then acquired to create a qualitative map of its geometry and to ensure its morphologic

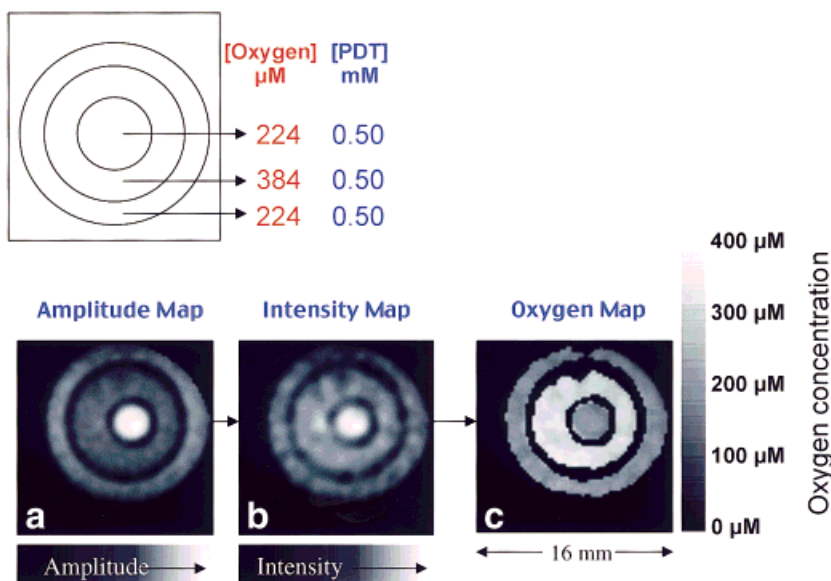


FIG. 3. Oxygen mapping in a three-tube bioreactor phantom. The phantom was constructed using three tubes in a concentric arrangement, as described in the text. The tubes were filled with 0.5 mM PDT. The inner- and outermost tubes were room-aerated (21%, 224  $\mu\text{M}$  oxygen) and filled with saline to a height of 4 cm. The solution in the middle tube was equilibrated with 36% (385  $\mu\text{M}$ ) oxygen, filled to a vertical height of 4 cm, and sealed. 3D spectral-spatial imaging data in the cross-sectional plane were collected, with the image obtained by filtered back-projection. **a:** 2D spatial map of spectral amplitudes corresponding to the resonance field. **b:** 2D spatial map of intensity obtained by integration over the spectral dimension. **c:** 2D map of oxygen obtained from line-width data. The scale on the right side of the oxygen map shows the calibrated oxygen concentration ( $\mu\text{M}$ ). The image data acquisition parameters were as follows: projections = 576; FOV =  $16 \times 16 \text{ mm}^2$ ; maximum gradient = 38.0 G/cm; acquisition time = 70 min.

symmetry and vertical alignment within the resonator. 3D imaging was also performed to visualize the distribution of the spin probe into the cartilage-filled HFBR.

#### Respiratory Chain Inhibition Experiments

The HFBR containing cartilage was centered in the resonator and perfused with TCM containing 1.0 mM PDT, as described above. Spectra were acquired every 3 min. Data acquisition of spectral-spatial images began after 20 min of perfusion, allowing sufficient time for the spin probe to completely distribute into the cartilage.

The bioreactor was then perfused with 10 mM cyanide (5). EPR spectra of the entire sample were acquired until steady-state signal line-width and amplitude had been reached. This was followed by 3D spectral-spatial image acquisitions.

## RESULTS

### Three-Concentric-Tube Phantom

To validate the application of the EPROM technique to cartilage in an HFBR, we performed experiments using nitroxides in phantoms. Figure 3 shows 3D spectral-spatial images of a three-tube phantom designed to approximate the geometry of the HFBR. Spatial maps are displayed that correspond to 1) absorption line amplitude at the resonance field, 2) signal intensity as measured by integration over the absorption line, and 3) oxygen. The reentrant resonator used for the imaging experiments had an active spherical volume with a diameter of approximately 20 mm, while the overall cross-sectional dimension of the phantom was fully 16 mm. Although the three tubes in the phantom were each filled to a height of 40 mm and centered in the active volume of the resonator, the projection onto the horizontal plane of the EPR spin probe density weighted by the local resonator sensitivity was nonuniform. Thus, the innermost tube appears brighter than the outermost tube in the amplitude and intensity maps despite having an equal concentration of probe and oxygen. However, the profiling is not evident in the 3D spectral-spatial or 3D spatial experiments reported below, as the cross-sectional size of the cartilage is small compared to the size of the resonator.

The profiling effect is absent from the oxygen maps, as line-width is independent of the resonator sensitivity. Indeed, in the derived oxygen map of the phantom, the inner- and outermost tubes have equal brightness, corresponding to approximately 200  $\mu\text{M}$  oxygen, and accurately reflecting the phantom construction. The calculated oxygen concentration in the middle tube is approximately 350  $\mu\text{M}$ , which also agrees well with its actual value. Thus, the EPROM map, constructed from amplitude and intensity maps, provides information about line-width that is independent of probe concentration. Because line-width increases with increasing oxygen concentration, the middle tube appears to be brighter on the oxygen map.

### Calibration

Figure 4 shows the results of the calibration experiments relating oxygen concentration ( $\mu\text{M}$ ) to paramagnetic line-broadening (mG). It is observed that oxygen produced a

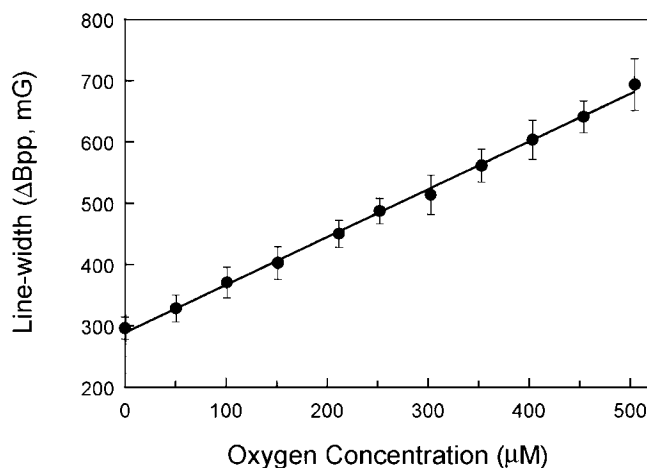


FIG. 4. Calibration of EPR line-broadening as a function of oxygen concentration ( $\mu\text{M}$ ). The oxygen calibration experiments were performed at room temperature. The observed broadening (peak-to-peak line widths;  $\Delta\text{Bpp}$ ) varied almost linearly from 290 mG at 0  $\mu\text{M}$  oxygen to 680 mG at 500  $\mu\text{M}$  oxygen. The dependence of line-width on oxygen was described by line-width (mG) =  $290 + 0.78 \pm 0.04 \text{ mG} \times [\text{O}_2] (\mu\text{M})$ .

linear line-width variation approximated by  $0.78 \pm 0.04 \text{ mG}/\mu\text{M}$  oxygen.

While PDT partitions more into lipids than does PCA, the EPROM technique effectively factors out any dependency of measured oxygen concentration on local spin probe concentration. The calibration can therefore be used to determine local oxygen concentrations in systems with various spin-probe types and concentrations.

### Influx/Efflux Experiment

Figure 5 shows the results of imaging the perfusion of PDT into and out of a bioreactor filled with TCM. The scale below the figure indicates the relative signal intensity given by increasing concentrations of the spin-probe inside the bioreactor.

Images of inflow indicate that it takes approximately 13 min before the probe enters the bioreactor. At that time, the bright central region corresponds to PDT flowing through the perfusion fiber. It takes approximately 19 min before the probe becomes uniformly distributed throughout the bioreactor.

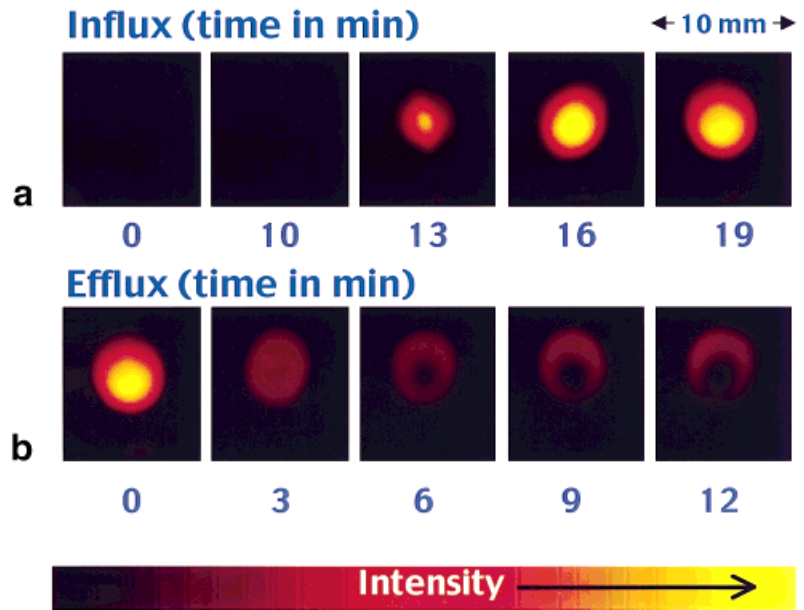
The washout images indicate that the nitroxide is cleared quickly during perfusion of the medium without a spin probe. The PDT in the central fiber is washed away immediately and signal within the reactor is substantially decreased as early as 3 min. Fifteen min after the beginning of the washout experiment, there is minimal detectable PDT left in the reactor. Together, these influx and efflux experiments indicate the approximate time course for PDT infusion into and out of the perfusion fiber and the entire HFBR volume itself.

### Cartilage Experiments

#### 3D Imaging of Cartilage

To visualize the distribution of the nitroxide label inside the cartilage-filled bioreactor, 3D spatial imaging experi-

FIG. 5. EPR imaging of nitroxide uptake and clearance in the bioreactor. **a:** 1.0 mM PDT was infused along with TCM, and 2D spatial images of the bioreactor were obtained continuously. **b:** After equilibration was reached, the reactor was perfused with only the TCM while a series of 2D spatial images were acquired until the nitroxide was fully cleared. The image data acquisition parameters were as follows: projections = 32; FOV = 10 × 10 mm<sup>2</sup>; gradient = 10 G/cm; acquisition time = ~2.5 min per image.



ments were performed. Figure 6 shows longitudinal and transverse images of the nitroxide (PCA) distribution in tissue grown in a bioreactor. The scale to the right indicates the relative amount of PCA (in arbitrary units) that has distributed into the bioreactor.

The central perfusion fiber which runs along the entire length of the cylindrical sleeve of cartilage can readily be seen in the longitudinal slices, and appears brighter than the cartilage. The spin probe is largely excluded from the intracellular component of the cartilage, which forms a significant fraction of the tissue. Accordingly, the probe is

more concentrated in the central perfusion fiber, making the center of the image brighter. The regions immediately around the fiber, which share voxels with the central fiber, also appear brighter due to a partial volume effect.

The tissue region is also readily observed, indicating that the probe has diffused into the cartilage. The radial projection of tissue at the bottom of the image represents cartilage that grew into and filled the side port used for chondrocyte injection. The transverse slices show the bright central fiber, the radial projection of cartilage in the side port, and the cylindrical symmetry of tissue growth.

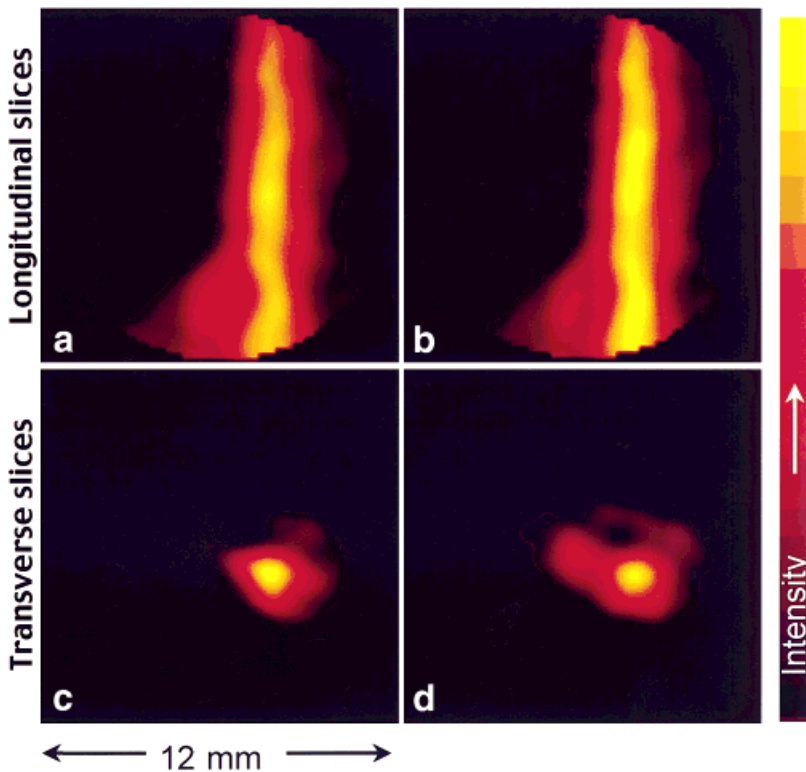


FIG. 6. 3D imaging of nitroxide distribution in the HFBR. The bioreactor was perfused with the TCM containing 1.0 mM of PCA. **a, b:** Longitudinal slices showing symmetric growth around a central perfusion fiber and cartilage growing into the injection port. **c, d:** Transverse slices showing cross-sectional views of perfusion fiber and cartilage. The image data acquisition parameters were as follows: projections = 256; FOV = 12 × 12 × 12 mm<sup>3</sup>; gradient = 10 G/cm; acquisition time = 18 min.

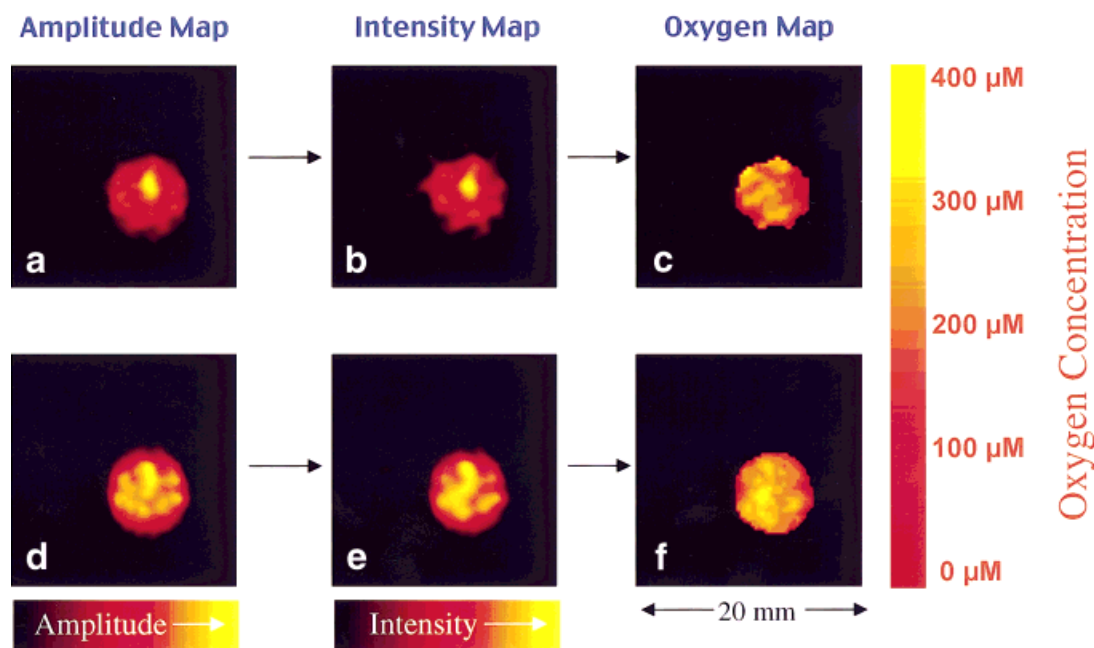


FIG. 7. Oxygen mapping in cartilage grown in an HFBR. The reactor was perfused with 1.0 mM PDT, and 3D spectral-spatial imaging in the cross-sectional plane of the reactor was performed. **a–c**: Amplitude, intensity, and oxygen mapping of the bioreactor perfused with TCM and PDT. **d–f**: Amplitude, intensity, and oxygen mapping of the reactor after treatment of the bioreactor perfused with TCM, PDT, and cyanide. The oxygen map of cyanide-treated cartilage appears brighter than the control; quantitative analysis showed an increase in oxygen concentration from 225  $\mu\text{M}$  to 310  $\mu\text{M}$  after treatment with cyanide. The image data acquisition parameters were as follows: projections = 576; FOV =  $20 \times 20 \text{ mm}^2$ ; maximum gradient = 21.7 G/cm; acquisition time =  $\sim 70$  min.

### Respiratory Chain Inhibition Experiments

To measure the changes in tissue oxygenation under conditions that alter oxygen consumption rates, experiments were performed in which cyanide was used to inhibit the respiratory chain. Cyanide is known to inhibit cytochrome c of the mitochondrial respiratory chain, thus decreasing oxygen consumption. Figure 7 shows the EPROM experiments performed on control and cyanide-treated cartilage. The central perfusion fiber can be seen on both the amplitude and intensity maps of control and cyanide-treated cartilage. Its disappearance on the oxygen maps confirms the rapid diffusion of oxygen into the tissue. No oxygen gradient within the cartilage can be observed in either oxygen map. The oxygen map obtained after the addition of cyanide to the tissue appears brighter than that obtained before cyanide. This qualitatively demonstrates the increased oxygen present in the cyanide-treated tissue, consistent with the inhibition of oxygen by cyanide. Average line-width values from the image indicate that there is significant line-broadening in cyanide-treated cartilage ( $0.50 \pm 0.03 \text{ G}$ ) compared with control ( $0.44 \pm 0.03 \text{ G}$ ) (Table 1). Oxygen concentrations were obtained from the line-broadening values using data from the calibration experiments. Quantitatively, we found that tissue oxygen concentration after cyanide treatment (310  $\mu\text{M}$ ) was significantly higher than before treatment (225  $\mu\text{M}$ ).

### DISCUSSION

Cartilage is an avascular tissue that relies primarily upon anaerobic respiration to produce energy (10). The presence

of oxygen, however, is crucial to its function (1–5,7,9). Cyanide is a potent inhibitor of cytochrome c and therefore decreases aerobic respiration. In contrast, reactive oxygen species (ROS) can damage chondrocytes and degrade matrix in various arthritic conditions (43). These ROS generally combat pathogens, but are also thought to be able to damage normal host cells (44–47). Oxygen is therefore a central parameter in cartilage metabolism.

We have shown that EPROM can be applied to map oxygen concentration in cartilage grown in three dimensions in an HFBR. Methods that utilize microelectrodes can also provide such information, but are invasive. Unlike the other EPR methods for oxygen measurements mentioned in the Introduction, the EPROM technique provides localized information specific to regions of interest within the tissue (30–35).

The oxygen map obtained using EPROM provides useful qualitative information regarding tissue oxygen distribution. Areas of tissue with higher oxygen concentrations

Table 1  
Line-Broadening and Oxygen Concentration in Cartilage Before and After Treatment With Cyanide

	Before cyanide	After cyanide
Line-width (G) <sup>a</sup>	$0.44 \pm 0.03$	$0.50 \pm 0.03$
Oxygen concentration ( $\mu\text{M}$ ) <sup>b</sup>	225	310

<sup>a</sup>Average line-broadening values calculated by taking mean of line-width values on oxygen maps (both before and after cyanide).

<sup>b</sup>Oxygen content calculated from calibration of EPR line-broadening as a function of oxygen concentration.

appear brighter while those with lower concentrations appear darker, as seen in the image of the cyanide-treated cartilage sample. EPROM also provides quantitative information about local oxygen concentrations. Using a calibration curve, line-width information at any given voxel can be used to obtain oxygen concentrations. We found that the provision of cyanide to our cartilage sample increases the oxygen concentration in cartilage to 310  $\mu\text{M}$  from the 225  $\mu\text{M}$  baseline.

The concentration of oxygen in the cartilage studied is in the same physiologic range as obtained previously in the in vivo rat tail (1). As discussed in both cases, the higher solubility of oxygen in lipid does not present a specific difficulty with the EPROM technique when concentrations of oxygen are expressed in micromolar ( $\mu\text{M}$ ) units.

In principle, EPROM should be able to define oxygen concentration gradients within tissue. However, a gradient was not detected in the cartilage experiments. This may be due to several factors. First, the measurements are non-slice-selective, so that minor sample placement asymmetry, or intrinsic asymmetry in the sample itself, would limit the apparent difference between two points in the image projected onto the plane transverse to the long axis of the bioreactor. Second, there is a limited intrinsic spectral resolution of the EPROM method, as implemented here, and therefore an oxygen gradient detection threshold exists.

A third limitation can be appreciated by examination of the phantom data shown in Fig. 3, in which it is evident that even in well mixed compartments with uniform oxygen concentration there is some apparent heterogeneity in the EPROM data. This is due to the limited signal-to-noise ratio of the experiment. Thus, a small gradient may indeed be present across the bioreactor that is below the threshold for detection by EPROM.

The presence of small oxygen concentration nonuniformities in the tissue can not be ruled out due to potential small local variations in cellularity. Despite the lack of a detectable gradient, there is sufficient oxygen consumption by the cells to cause an increase in measured oxygen after the addition of cyanide across the bioreactor, taken as a whole.

A limitation of EPROM as applied to the present study was the restriction of localization to two dimensions. Nevertheless, we were able to study the radial distribution of oxygen due to the axially symmetric geometry of the HFBR. The requirement of particular sample geometry can be overcome by implementing EPROM in three spatial dimensions and one spectral dimension, at the expense of increased imaging time. Other alternatives include implementing slice-selective imaging or the use of an appropriate resonator geometry (31).

## ACKNOWLEDGMENTS

We thank Kenneth W. Fishbein for his technical help, and two referees for their useful comments.

## REFERENCES

- Nahir AM. Aerobic glycolysis: a study of human articular cartilage. *Cell Biochem Funct* 1987;5:109–112.
- Marcus RE. The effect of low oxygen concentration on growth, glycolysis, and sulfate incorporation by articular chondrocytes in monolayer culture. *Arthritis Rheum* 1973;16:646–656.
- Lane JM, Brighton CT, Menkowitz BJ. Anaerobic and aerobic metabolism in articular cartilage. *J Rheumatol* 1977;4:334–342.
- Obradovic B, Carrier RL, Vunjak-Novakovic G, Freed LE. Gas exchange is essential for bioreactor cultivation of tissue engineered cartilage. *Biotechnol Bioeng* 1999;63:197–205.
- Lee RB, Urban JP. Evidence for a negative Pasteur effect in articular cartilage. *Biochem J* 1997;321:95–102.
- Rajpurohit R, Koch CJ, Tao Z, Teixeira CM, Shapiro IM. Adaptation of chondrocytes to low oxygen tension: relationship between hypoxia and cellular metabolism. *J Cell Physiol* 1996;168:424–432.
- Ishihara H, Urban JP. Effects of low oxygen concentrations and metabolic inhibitors on proteoglycan and protein synthesis rates in the intervertebral disc. *J Orthop Res* 1999;17:829–835.
- Otte P. Biology of articular cartilage with special reference to transplantation. *Z Orthop Ihre Grenzgeb* 1972;110:677–685.
- Shapiro IM, Mansfield KD, Evans SM, Lord EM, Koch CJ. Chondrocytes in the endochondral growth cartilage are not hypoxic. *Am J Physiol* 1997;272:C1134–C1143.
- Urban JP, Holm S, Maroudas A, Nachemson A. Nutrition of the intervertebral disc: effect of fluid flow on solute transport. *Clin Orthop* 1982;296–302.
- Silverton SF, Wagerle LC, Robiolo ME, Haselgrove JC, Forster RE. Oxygen supply to the cartilage growth plate: an estimation of oxygen gradients in two regions of the epiphyseal growth plate. In: Rakusan E, editor. *Oxygen transport to tissue*, vol. IX. New York: Plenum Press; 1989. p 809–815.
- Mow VC, Ratcliffe A, Poole AR. Cartilage and diarthrodial joints as paradigms for hierarchical materials and structures. *Biomaterials* 1992; 13:67–97.
- Reginato AM, Iozzo RV, Jimenez SA. Formation of nodular structures resembling mature articular cartilage in long-term primary cultures of human fetal epiphyseal chondrocytes on a hydrogel substrate. *Arthritis Rheum* 1994;37:1338–1349.
- Potter K, Fishbein KW, Horton WE, Spencer RGS. Morphometric analysis of cartilage grown in a hollow fiber bioreactor using NMR microscopy. In: Blümler P, Blümler B, Botto R, Fukushima E, editors. *Spatially resolved magnetic resonance: methods, materials, medicine, biology, rheology, geology, ecology, hardware*. Weinheim: Wiley-VCH Press; 1998. p 363–371.
- Petersen EF, Fishbein KW, McFarland EW, Spencer RG. 31P NMR spectroscopy of developing cartilage produced from chick chondrocytes in a hollow-fiber bioreactor. *Magn Reson Med* 2000;44:367–372.
- Petersen E, Potter K, Butler J, Fishbein KW, Horton W, Spencer RGS, McFarland EW. Bioreactor and probe system for magnetic resonance microimaging and spectroscopy of chondrocytes and neocartilage. *Int J Imaging Syst Technol* 1997;8:285–292.
- Potter K, Butler JJ, Adams C, Fishbein KW, McFarland EW, Horton WE, Spencer RG. Cartilage formation in a hollow fiber bioreactor studied by proton magnetic resonance microscopy. *Matrix Biol* 1998;17:513–523.
- Potter K, Butler JJ, Horton WE, Spencer RG. Response of engineered cartilage tissue to biochemical agents as studied by proton magnetic resonance microscopy. *Arthritis Rheum* 2000;43:1580–1590.
- Benya PD, Shaffer JD. Dedifferentiated chondrocytes reexpress the differentiated collagen phenotype when cultured in agarose gels. *Cell* 1982;30:215–224.
- Elima K, Vuorio E. Expression of mRNAs for collagens and other matrix components in dedifferentiating and redifferentiating human chondrocytes in culture. *FEBS Lett* 1989;258:195–198.
- Stewart MC, Saunders KM, Burton-Wurster N, Macleod JN. Phenotypic stability of articular chondrocytes in vitro: the effects of culture models, bone morphogenetic protein 2, and serum supplementation. *J Bone Miner Res* 2000;15:166–174.
- Stefanovic-Racic M, Stadler J, Georgescu HI, Evans CH. Nitric oxide and energy production in articular chondrocytes. *J Cell Physiol* 1994; 159:274–280.
- Macpherson JV, O'Hare D, Unwin PR, Winlove CP. Quantitative spatially resolved measurements of mass transfer through laryngeal cartilage. *Biophys J* 1997;73:2771–2781.
- Bartels EM, Fairbank JC, Winlove CP, Urban JP. Oxygen and lactate concentrations measured in vivo in the intervertebral discs of patients with scoliosis and back pain. *Spine* 1998;23:1–7; discussion 8.

25. Lund-Olesen K. Oxygen tension in synovial fluids. *Arthritis Rheum* 1970;13:769–776.
26. Haselgrove JC, Shapiro IM, Silverton SF. Computer modeling of the oxygen supply and demand of cells of the avian growth cartilage. *Am J Physiol* 1993;265:C497–C506.
27. Bartsch P, Strobl R, Hohnstadter G, Choinowski H, Krupp M, Pavel G. A Warburg apparatus with fully automatic recording of gas exchange in small biological objects with high stability of gas pressure. *Z Med Labortech* 1966;7:342–355.
28. Emel'ianov NA. A volumetric method for the measurement of gas consumption or liberation with the Warburg apparatus. *Ukr Biokhim Zh* 1971;43:390–392.
29. Misra MS, Nayak NR, Kundu AK. Relation between volume change and pressure change in oxygen uptake study using Warburg apparatus. *Indian J Exp Biol* 1991;29:872–874.
30. Halpern HJ, Yu C, Peric M, Barth E, Grdina DJ, Teicher BA. Oxymetry deep in tissues with low-frequency electron paramagnetic resonance. *Proc Natl Acad Sci USA* 1994;91:13047–13051.
31. Kuppusamy P, Afeworki M, Shankar RA, Coffin D, Krishna MC, Hahn SM, Mitchell JB, Zweier JL. In vivo electron paramagnetic resonance imaging of tumor heterogeneity and oxygenation in a murine model. *Cancer Res* 1998;58:1562–1568.
32. Kuppusamy P, Shankar RA, Zweier JL. In vivo measurement of arterial and venous oxygenation in the rat using 3D spectral-spatial electron paramagnetic resonance imaging. *Phys Med Biol* 1998;43:1837–1844.
33. James PE, Miyake M, Swartz HM. Simultaneous measurement of NO and PO<sub>2</sub> from tissue by in vivo EPR. *Nitric Oxide* 1999;3:292–301.
34. Swartz HM, Walczak T. Developing in vivo EPR oximetry for clinical use. *Adv Exp Med Biol* 1998;454:243–252.
35. Swartz HM, Dunn J, Grinberg O, O'Hara J, Walczak T. What does EPR oximetry with solid particles measure—and how does this relate to other measures of PO<sub>2</sub>? *Adv Exp Med Biol* 1997;428:663–670.
36. Swartz HM, Boyer S, Gast P, Glockner JF, Hu H, Liu KJ, Moussavi M, Norby SW, Vahidi N, Walczak T, Wu M, Clarkson RB. Measurements of pertinent concentrations of oxygen in vivo. *Magn Reson Med* 1991;20:333–339.
37. Halpern HJ, Spencer DP, Polen JV, Bowman MK, Nelson AC, Dowey EM, Teicher EA. Imaging radiofrequency electron spin resonance spectrometer with high resolution and sensitivity for in vivo measurements. *Rev Sci Instrum* 1989;60:1040–1050.
38. Kuppusamy P, Chzhan M, Vij K, Shteynbuk M, Lefer DJ, Giannella E, Zweier JL. Three-dimensional spectral-spatial EPR imaging of free radicals in the heart: a technique for imaging tissue metabolism and oxygenation. *Proc Natl Acad Sci USA* 1994;91:3388–3392.
39. Velan SS, Spencer RG, Zweier JL, Kuppusamy P. Electron paramagnetic resonance oxygen mapping (EPROM): direct visualization of oxygen concentration in tissue. *Magn Reson Med* 2000;43:804–809.
40. Zweier JL, Chzhan M, Samouilov A, Kuppusamy P. Electron paramagnetic resonance imaging of the rat heart. *Phys Med Biol* 1998;43:1823–1835.
41. Kuppusamy P, Zweier JL. A forward-subtraction procedure for removing hyperfine artifacts in electron paramagnetic resonance imaging. *Magn Reson Med* 1996;35:316–322.
42. Eaton GR, Eaton SS, Ohno K. EPR imaging and in vivo EPR. Boca Raton: CRC Press, Inc.; 1991.
43. Greenwald RA. Oxygen radicals, inflammation, and arthritis: pathophysiological considerations and implications for treatment. *Semin Arthritis Rheum* 1991;20:219–240.
44. Bates EJ, Harper GS, Lowther DA, Preston BN. Effect of oxygen-derived reactive species on cartilage proteoglycan-hyaluronate aggregates. *Biochem Int* 1984;8:629–637.
45. Tiku ML, Gupta S, Deshmukh DR. Aggrecan degradation in chondrocytes is mediated by reactive oxygen species and protected by antioxidants. *Free Radic Res* 1999;30:395–405.
46. Fragonas E, Pollesello P, Mlinarik V, Toffanin R, Grando C, Godeas C, Vittur F. Sensitivity of chondrocytes of growing cartilage to reactive oxygen species. *Biochim Biophys Acta* 1998;1425:103–111.
47. Kurz B, Steinhagen J, Schunke M. Articular chondrocytes and synovio-cytes in a co-culture system: influence on reactive oxygen species-induced cytotoxicity and lipid peroxidation. *Cell Tissue Res* 1999;296:555–563.